Available online at www.sciencedirect.com
SCIENCE DIRECT®
Journal of Sound and Vibration 270 (2004) 573–586
JOURNAL OF SOUND AND VIBRATION
www.elsevier.com/locate/jsvi

A numerical method for computation of sound radiation from an unflanged duct

X.X. Chen[a,*], X. Zhang[b], C.L. Morfey[a], P.A. Nelson[a]

[a] *Institute of Sound and Vibration Research, University of Southampton, Southampton SO17 1BJ, UK*
[b] *School of Engineering Sciences, University of Southampton, Southampton SO17 1BJ, UK*

Accepted 15 September 2003

Abstract

Some issues involved in establishing a numerical model for sound radiation from a straight duct are addressed in this paper. The main ingredient of the numerical method is solutions of linearized Euler equations using a high order compact scheme. Farfield directivity is estimated through an integral solution of Ffowcs–Williams Hawkings equations. A generic test case of planar wave radiation from an unflanged duct is studied. The sound pressure level and wave propagation in the nearfield are analyzed, together with the farfield directivity. Comparison with analytical solutions shows good agreement. The effect of grid resolution on the sound radiation pattern and the construction of integration surface on the farfield directivity are discussed.

1. Introduction

Sound radiation from an engine inlet duct is a challenging problem in aeroacoustics. Numerical models based on finite element/infinite element methods have been developed for problems. Recently, methods based on computational aeroacoustics (CAA) have also been developed. CAA is concerned predominately with obtaining time-accurate numerical solutions to unsteady flow and acoustic problems, through application of long-time accurate time-integration strategies and high order spatial discretization schemes to the flow governing equations. A variety of issues need to be addressed in attempting a numerical simulation of the aeroacoustic problem, such as non-dissipative and non-dispersive requirements for acoustic waves, which have small amplitude and high frequency compared to mean flows, non-reflecting boundary conditions and long-time

*Corresponding author. Tel.: +44-23-8059-2321.
E-mail address: xxc@soton.ac.uk (X.X. Chen).

0022-460X/$ - see front matter
doi:10.1016/j.jsv.2003.09.055

history at large distances [1]. Over years a number of studies have appeared dealing with different aspects of the duct radiation problem [2–8]. Özyörük and Long [2] used a temporally and spatially fourth order accurate, three-dimensional (3D) Euler solver coupled with the Kirchhoff method to predict the farfield sound pressure. They showed that a grid resolution of 12 points-per-wavelength (PPW) gave results without significant dispersion and dissipation. However the accuracy of the Kirchhoff method depends on the surfaces. Wells and Renaut [3] provided an overview of the problem associated with aerodynamically generated noise. Using a sixth order spatial scheme, they found that a 6 PPW (minimum 4 PPW) calculation resulted in a slightly slower wave speed compared with accurate solution. However a 8 PPW calculation gave quite accurate results. With a second order scheme, 50 PPW would be needed for good results. Rumsey et al. [4] used a Navier–Stokes code (CFL3D) together with the Kirchhoff method to predict farfield sound pressure from ducted-fan engine acoustic modes. In their calculation, 25 PPW spatial resolution was required for the second order accurate code.

In this paper, some issues involved in developing a radiation model based on CAA are discussed. The specified test case is the modal radiation (with and without mean flow) problem described by Homicz and Lordi [9]. In particular, a planar wave radiation computation to simplify the computation setup is selected. For this case, farfield analytical solutions exist and nearfield solutions can be obtained from existing finite element methods. Therefore, both the nearfield and farfield CAA predictions can be validated. The specific strategy is based on CAA algorithms running on parallel computing platforms, combining aeroacoustic treatment of boundaries for wave admission and emission, a high order compact scheme with low dispersion and dissipation errors for propagation, and acoustic analogy models for farfield radiation. Attention has been paid to issues such as the size of the buffer zone for various acoustic wave inputs and outputs, the placement of the integration surface, and the grid resolution around the duct edge. At every step the nearfield and farfield predictions are compared with existing solutions, either analytical or numerical. In the paper, however, only the farfield comparisons are shown.

2. Method

2.1. Numerical model

As illustrated in Fig. 1 the whole computational domain is divided into three regions: the wave admission and emission regions, a propagation region around the edge of the duct and a radiation region outside the propagation region. The CAA model is applied to these regions with specific emphasis. Through the wave admission region, prescribed incoming waves from either duct acoustic calculation or computational fluid dynamics (CFD) calculation are admitted into the propagation region, in a form defined later. Spurious waves in the wave admission and emission regions are damped by using a buffer zone boundary condition. In the propagation region, the acoustic wave propagation is predicted by solutions of the linearized Euler equations (LEE). The background mean flow can be a CFD solution, a measurement or an analytical solution. The LEE solution also provides input to the radiation model which is applied to the wave radiation region. In this study, an integral solution of the FW–H equation [10] is used to predict the farfield radiation.

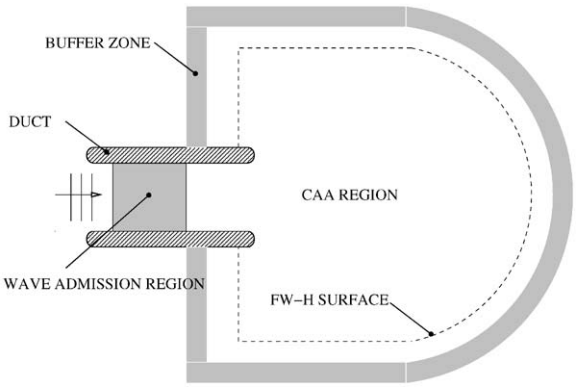

Fig. 1. Schematic of the radiation model.

2.2. Linearized Euler equations

Assuming small perturbations about a steady mean flow, the acoustic wave propagation can be described by the LEE:

$$\frac{\partial \rho'}{\partial t} = -\left(\mathbf{v}_0 \cdot \nabla \rho' + \mathbf{v}' \cdot \nabla \rho_0 + \rho_0 \nabla \cdot \mathbf{v}' + \rho' \nabla \cdot \mathbf{v}_0 + \alpha_1 \frac{\rho' v_0 + \rho_0 v'}{y}\right), \tag{1}$$

$$\frac{\partial u'}{\partial t} = -\left(\mathbf{v}_0 \cdot \nabla u' + \mathbf{v}' \cdot \nabla u_0 + \frac{1}{\rho_0}\frac{\partial p'}{\partial x}\right), \tag{2}$$

$$\frac{\partial v'}{\partial t} = -\left(\mathbf{v}_0 \cdot \nabla v' + \mathbf{v}' \cdot \nabla v_0 + \frac{1}{\rho_0}\frac{\partial p'}{\partial y} - \alpha_1 \frac{2w'w_0}{y}\right), \tag{3}$$

$$\frac{\partial w'}{\partial t} = -\left(\mathbf{v}_0 \cdot \nabla w' + \mathbf{v}' \cdot \nabla w_0 + \frac{1}{\rho_0}\frac{\partial p'}{\partial z} + \alpha_1 \frac{v_0 w' + v' w_0}{y}\right), \tag{4}$$

$$\frac{\partial p'}{\partial t} = -\left[\mathbf{v}_0 \cdot \nabla p' + \mathbf{v}' \cdot \nabla p_0 + \gamma\left(p_0 \nabla \cdot \mathbf{v}' + p' \nabla \cdot \mathbf{v}_0 + \alpha_1 \frac{p' v_0 + p_0 v'}{y}\right)\right], \tag{5}$$

where ρ', $\mathbf{v}'$, p' are density, velocity and pressure perturbations, ρ_0, $\mathbf{v}_0$, p_0 are mean flow properties and $\alpha_1 = 0$ for a Cartesian co-ordinate system. In cylindrical co-ordinates, $\alpha_1 = 1$ and the derivative $\partial/\partial z$ in Eqs. (1)–(5) is replaced by $\partial/(y\partial\theta)$, where θ is the azimuthal angle. The fluid is modelled as a perfect gas, and all variables are non-dimensionalized using a length scale of 1 m, a velocity scale of 340 m/s and a density of 1.225 kg/m^3. In presenting the results, unless otherwise stated non-dimensional values will be used.

2.3. Non-reflecting boundary conditions

The numerical scheme employed in the study possesses low dissipation and dispersion characteristics. Hence any inconsistencies due to numerical treatments in the inflow and outflow

boundaries will introduce errors or spurious wave reflections in the computation, which will eventually degrade the solutions. In the buffer zone, damping is directly applied to the numerical solution vector $\mathbf{Q} = (\rho', u', v', w', p')^{\mathrm{T}}$ at each time step,

$$\tilde{\mathbf{Q}} = \mathbf{Q} - \sigma(\mathbf{Q} - \mathbf{Q}_{target}), \tag{6}$$

where $\mathbf{Q}_{target}$ is a given reference. The damping coefficient σ is defined as

$$\sigma(l) = \alpha_2 \left(\frac{L - l}{L}\right)^{\beta_1}, \tag{7}$$

where l is the distance from outer boundary of the buffer zone, L is the buffer zone width. Parameters α_2 (= 1) and β_1 (= 1.5) are used to determine the nature of the damping coefficient σ which varies smoothly from zero at the interface between the buffer zone and propagation region to a value, normally one, at the outer boundary. The specified damping coefficient provides a sufficient amount of damping to filter spurious reflections. An investigation by Richards et al. [11] shows that, among various types of non-reflecting boundary conditions, the explicit formulation used in this work is better suited for duct radiation computation.

Within the wave admission region, waves, other than the incoming waves, will be damped. This allows the integrity of the acoustic inflow condition to be maintained. Within the wave emission region the buffer zone boundary condition is also used to prevent the reflected waves from the outer boundaries by setting the reference values to zero since the exact wave solution is unknown. This is critical for accurate farfield noise radiation computations using an integral method.

2.4. Radiation model

An integral solution of the FW–H equation has been implemented numerically to allow the farfield noise level to be determined efficiently. The particular integral solution implemented is known as formulation 1A following Farassat [12]. This time-domain formulation is valid in both the near- and far fields, and is appropriate for surfaces in arbitrary motion.

3. Numerical implementation and code validation

The LEE solver uses a sixth order compact scheme [13] for spatial derivatives and a fourth order 4/6 stage explicit Runge–Kutta scheme [14] in time integration. In order to filter the small numerical disturbances a 10th order filter is also applied at each stage of the Runge–Kutta scheme [15]. The propagating unsteady flow perturbations (ρ', u', v', w', p') are then recorded in the integration surface, which is placed within the LEE computational domain, as inputs to the FW–H solver. A slip-wall boundary condition is applied to the duct wall surface and the buffer zones are placed around the outer boundary of the physical computational domain as non-reflecting boundary conditions to filter out the reflected waves. A symmetric boundary condition may be applied depending on problem specified. Only 2D problems are considered here.

However the application to 3D problems is straightforward and the code is written to enable this extension.

In evaluating the farfield noise level, a 3D integration surface is constructed. The azimuthal grid number is fixed at 40 for zero azimuthal mode to retain accurate 3D data for the FW–H prediction. To assess the farfield directivity, the analytical solution of Homicz and Lordi [9] is given at a distance of 100 m from a center at $(x_e, 0)$ where x_e is the axial value at the duct edge. The solutions cover an arc of 120° consisting of 100 points.

The basic methodology has been validated against a range of test cases, including a Gaussian pulse passing though a 2D cylinder [13] and linear wave propagation problems. Good agreements have been found.

4. Planar wave radiation from an unflanged duct

4.1. Problem set up

A single (m, n) mode, where azimuthal mode number $m = 0$ and $n = 1$ is first zero of the Bessel function of zeroth order of first kind, is used as an input for the modal propagation and radiation from a semi-infinite unflanged duct with infinitive thin rigid wall against an uniform mean flow: constant u_0 and p_0, $w_0 = 0$ and $v_0 = 0$. The incident acoustic wave is also axisymmetrical ($w' = 0$). The effect of wall thickness [8], although investigated in the study, is not reported here.

The computational domain is shown in Fig. 2, which represents a cross section of the 3D semi-infinite circular duct. The radius of the duct is 1 m. Since the geometry is symmetric about the duct axis, only half of the duct is used in the computation. A fine uniform grid ($\Delta x = \Delta y = 0.019$) is firstly established and it has 33 PPW grid resolution in the axial direction without mean flow. A total of 55 400 grid cells is used. Stretched grids are also used and will be presented in later sections. In monitoring solution convergence, results along a 2 m radius arc, with its center at $(x_e, 0)$, and angle ϕ ranging from 0° to 120°, are compared after each incident wave period (Fig. 3). A relative error of 1% is used as the convergence criterion. For the uniform grid without mean flow, a computational time of 35 incident wave periods is sufficient for solution convergence.

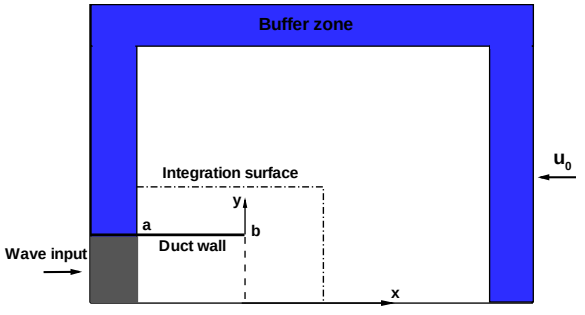

Fig. 2. Schematic of an unflanged duct domain and buffer zones.

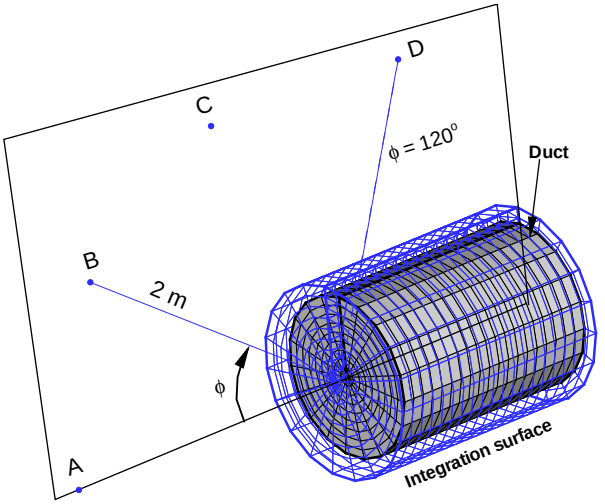

Fig. 3. Illustration of a 3D FW–H integration surface.

In the wave admission region the incident acoustic wave in the whole buffer zone is defined for a (0,1) mode in a circular duct as

$$
\begin{aligned}
p'(x,y,t) &= aJ_0(k_r y)\mathrm{Re}[e^{i(kt-k_a x)}],\\
\rho'(x,y,t) &= p'(x,y,t),\\
u'(x,y,t) &= \frac{k_a}{(k-k_a u_0)}p'(x,y,t),\\
v'(x,y,t) &= \frac{a}{(k-k_a u_0)}\frac{dJ_0(k_r y)}{dy}\mathrm{Re}[e^{i(kt-k_a x+\pi/2)}],\\
w'(x,y,t) &= 0,
\end{aligned}
\tag{8}
$$

where the wave amplitude a is fixed at 10^{-4} to ensure small pressure perturbation to the mean pressure $1/\gamma$ ($\simeq 0.71$) and the frequency is $k = 11$ (595 Hz). The radial wavenumber k_r is determined by turning points of the Bessel function. The axial modal number k_a and cut-off ratio ξ are calculated from

$$
k_a = \frac{k}{\beta^2}\left(-u_0 + \sqrt{1-\xi^{-2}}\right) \quad \text{and} \quad \xi = \frac{k}{k_r\beta},
$$

where $\beta = \sqrt{1-u_0^2}$ and k_a is positive for upstream-moving wave and $u_0 \leqslant 0$.

4.2. *Effect of the buffer zone as a non-reflecting condition*

For the present case, the outgoing disturbances in the admission region come mainly from the duct edge. The wave reflections from the wave emission region are ignored in the analysis since they are less important due to much weak wave magnitude. In fact, the shape/placement of the buffer zone in the wave emission region can be manipulated to minimize the reflections.

Acoustic waves F' travelling inside the duct may be composed of three parts, the incident wave F'_i, the outgoing wave F'_o (towards the buffer zone) and the reflected wave F'_r from the buffer zone.

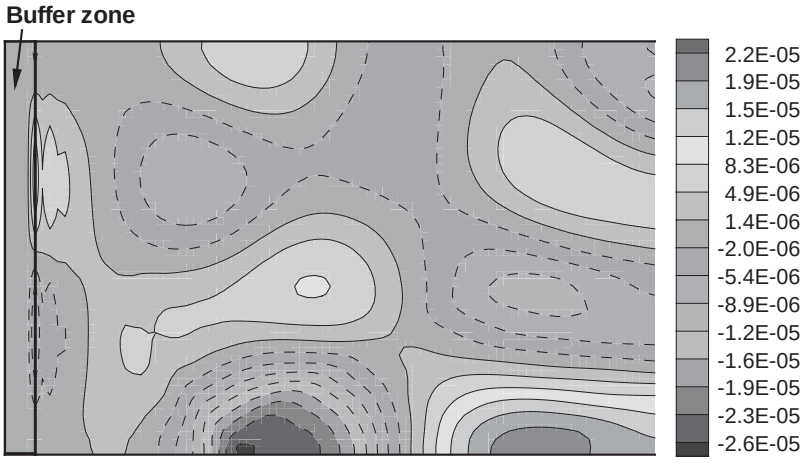

Fig. 4. Snapshot of $p' - p'_i$. $k = 11,\ u_0 = 0$.

The reflected wave F'_r should be much smaller than the other two waves after the buffer zone treatment. Since the outgoing waves may have a radial component, the time history of the pressure difference, $p' - p'_i$, in which p'_i is the known analytical solution, is monitored in the entire duct area to check the efficiency of the buffer zone condition. The reflected waves could be detected if the outgoing wave is contaminated. The effects of the buffer zone size on the wave reflection are examined in terms of the incident wavelength.

Richards et al. [11] have shown that the reflections from the buffer zone can be ignored if the wavefront angle is less than 30°. It is expected that same conclusion applies to the outgoing waves reflected from the duct edge if its wavefront angle is small. To check the buffer zone performance a number of buffer sizes have been tested using an uniform grid (33 PPW). The size of the buffer zone ranges from a minimum of 5 grid cells to 2 wavelengths (66 cells). No apparent reflections are observed in these tests. Fig. 4 shows a snapshot of the pressure difference for the buffer size of 5 cells. In one typical wave period all pressure differences move towards the buffer zone and their levels are reduced in the buffer zone. High accuracy of the scheme means that the propagating wave will almost be retained. Therefore, the spurious waves should be detected in the wave propagating region if they are not filtered in the buffer zone and reflected. The fact of no apparent trace of the reflected waves indirectly confirms that there are no significant wave reflections from the buffer zone.

The wavefront angle of the outgoing wave depends on the cut-off ratio ξ. A smaller cut-off ratio will result in a larger wavefront angle. In this case, the cut-off ratio is 2.87 and wavefront angle of the incident wave is about 20.4°. As the minimum buffer size has been successfully used in this test, the wavefront angle of the outgoing wave may be less than 20.4°.

4.3. The integration surface placement

Placement and shape of the integration surface may affect the prediction accuracy of the FW–H solver. In this study the integration surface is constructed based on the LEE computational grid

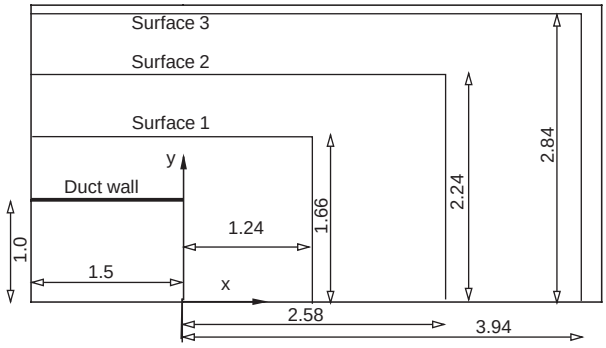

Fig. 5. Three FW–H integration surfaces.

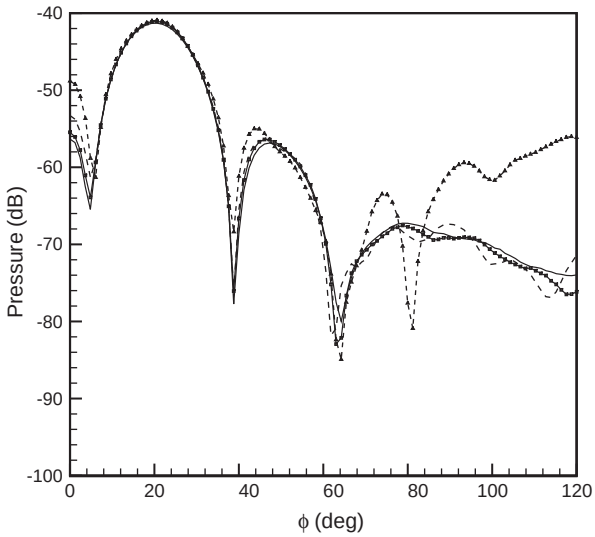

Fig. 6. Grid sensitivity test of Integration surface one. $\Delta x = 0.027,\ \Delta y = 0.019,\ u_0 = 0$. Solid line: 100% cells; solid line with square: 50% cells; dashed line: 25% cells; dashed line with triangle: 12.5% cells.

and uses the existing cells for the integration. Various surfaces with different integration cell densities can be used. Also the effectiveness of the non-reflection boundary condition could affect the information recorded on these surfaces, if they are placed close to the boundary. To study the effect, three integration surfaces shown on Fig. 5 are tested. The surface one is close to the duct and the surface three is close the wave emission regions.

Grid sensitivity is firstly tested using the information recorded on the surface one for one test case (23 PPW and $u_0 = 0$). Tests are conducted with the 100%, 50%, 25% and 12.5% of the grid cells on the surface. The base grid is an uniform, rectangular one with $\Delta x = 0.027,\ \Delta y = 0.019$. Results are presented in Fig. 6. It shows that half grid cells on the surface are sufficient for the directivity prediction. Small differences appear at high observation angle ϕ for the 50% cells. This difference in the farfield directivity level increases as the cell density is reduced. Different

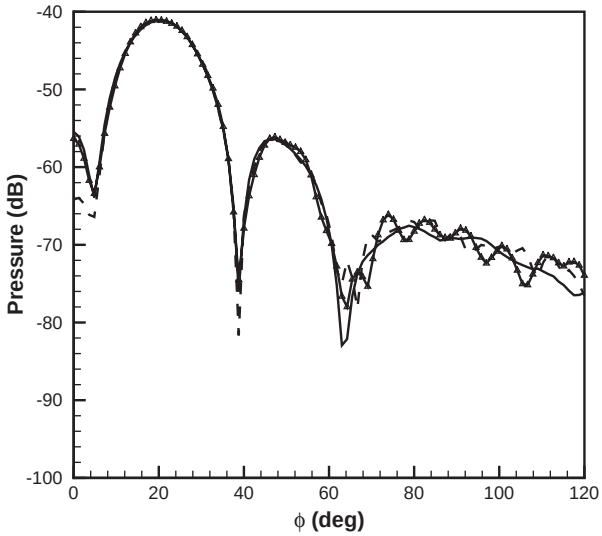

Fig. 7. Farfield directivity at 100 m using half grid cells in integration surface. Solid line: surface 1; solid line with triangle: surface 2; dashed line: surface 3.

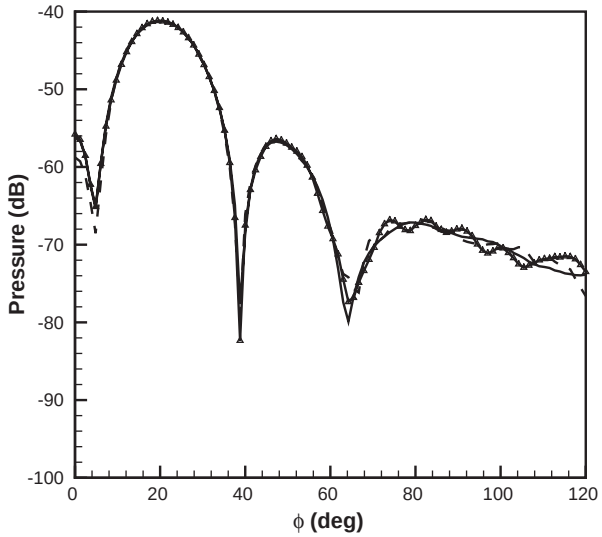

Fig. 8. Farfield directivity at 100 m using full grid cells in integration surface. Solid line: surface 1; solid line with triangle: surface 2; dashed line: surface 3.

behaviours at high and low angles may be caused by the difference in the size of the grid (Δx and Δy) in the axial and radial directions.

The farfield directivity patterns with various grid cells and surface placements are shown in Figs. 7 and 8. Main features such as the first two main radiation peaks and the interference dip angles are all well predicted for all surfaces. Such consistency is as expected due to the good performance of the buffer zone as non-reflecting boundary condition and the face that there is no

mean flow. It is observed that the predicted directivity from the surface one is the most accurate at high angle ϕ, suggesting that the surface one contains more information than the other two. The discrepancies in the directivity patterns at high angle between three surfaces are reduced when full grid cells are utilised (Fig. 8).

4.4. Grid resolution

Grid resolution affects the nearfield acoustic wave propagation and hence the farfield directivity. It is generally accepted that, for a high order scheme, a minimum of 6 PPW should be used in the computation. The minimum PPW requirement of course depends on specific spatial schemes. In this study, a baseline case is established using a very fine uniform grid (33 PPW). It is believed, however, that the high PPW requirement may only be needed in the immediate region around the edge of the duct where wave diffraction occurs. In this work a series of uniform grids are tested to find the minimum PPW requirement for accurate farfield directivity prediction, which are followed by a series of exercises using stretched grids around the edge of the duct. The aim is to reduce the overall grid resolution requirement yet maintain the same level of accuracy.

In the uniform grid study, grids with 5, 10, 15 and 33 PPW at $u_0 = 0$ are used, corresponding to the in-duct grid size of 13×55, 26×55, 37×55 and 83×55. When a mean flow of $u_0 = 0.5$, grids of 7, 16 and 30 PPW are tested. In the $u_0 = 0$ cases, results using grids of 15 and 33 PPW agree well with the analytical solutions (Figs. 9 and 10). Only a slightly lower level is observed in high observation angles ($\phi > 80$). In all four cases, main differences between the CAA predictions and the analytical solutions are in the high observation angles above 60°, which indicates the influence of the edge of the duct on the prediction quality. For the 5 PPW grid, there is a big drop in the pressure level (6.6 dB) and a large phase deviation, indicating an inadequate grid resolution. It appears that a minimum grid resolution around the edge of the duct should be around 15 PPW.

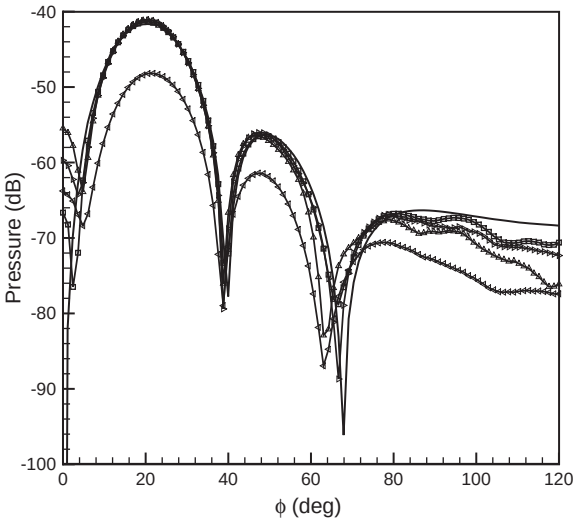

Fig. 9. Farfield directivity at 100 m without mean flow. Solid line: analytical solution; solid line with square: PPW = 33; solid line with right triangle: PPW = 15; solid line with triangle: PPW = 10; solid line with left triangle: PPW = 5.

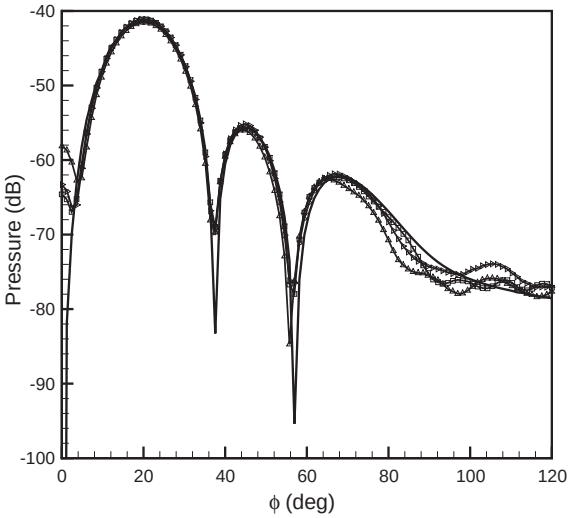

Fig. 10. Farfield directivity at 100 m with mean flow $u_0 = 0.5$. Solid line: analytical solution; solid line with square: PPW = 30; solid line with right triangle: PPW = 16; solid line with triangle: PPW = 7.

With the presence of a mean flow, the grid resolution requirement reduces. The grid resolutions drop from 15 and 33 PPW at $u_0 = 0$ to 7 and 16 PPW at $u_0 = 0.5$, respectively. The results show generally good agreement (Fig. 10) and a low grid resolution of 7 PPW now gives reasonable predictions.

A stretched grid is constructed using a transformation function in the axial and radial directions. The grid is compressed towards the duct wall in the radial direction and the edge of the duct in the axial direction. In the axial direction if x_1 is placed at the position a and $x_{\max}$ at the position b shown in Fig. 2, the transformation function is defined as

$$x_i = x_1 + (x_{\max} - x_1)\left[1 - \beta + \frac{2\beta}{1 + ((\beta+1)/(\beta-1))^{\psi}}\right], \tag{9}$$

where compression ratio $\beta > 1.0$, and $\psi = (i_{\max} - i)/i_{\max}$, $i = 1, 2, \ldots, i_{\max}$ where $i_{\max}$ is the maximum axial grid number and x_i is the corresponding axial coordinate value for index i. In this exercise, the cell size of the buffer zone is kept constant. Same procedure is used to form the stretched grid in the radial direction.

The grid stretching is performed on 5, 10 and 15 PPW uniform grids for the $u_0 = 0$ case and on the 7 PPW uniform grid for the $u_0 = 0.5$ case. As shown in Fig. 11 a stretched grid has an average 10 PPW resolution in the duct with minimum 6 PPW ($\Delta x = 0.1$, $\Delta y = 0.006$) and maximum 15 PPW ($\Delta x = 0.018$, $\Delta y = 0.006$) in the left and right sides of the duct.

A typical result using a stretched grid is shown in Fig. 12 for the $u_0 = 0$ and 10 PPW case. There appears a marked improvement in the directivity prediction, in both the level and angle. The improvement is especially good at high observation angles, though the predicted shadow interference dip angle is not sharp for the stretched grid. This is probably due to the coarse grid cells now used for the integration surface construction. In Fig. 13, the contours of nearfield pressure are plotted. The contour shapes of the pressure are very smooth except those associated

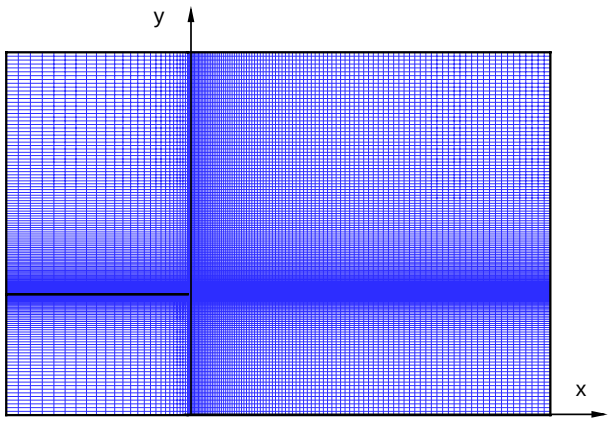

Fig. 11. Stretched grid (10 PPW, $u_0 = 0$).

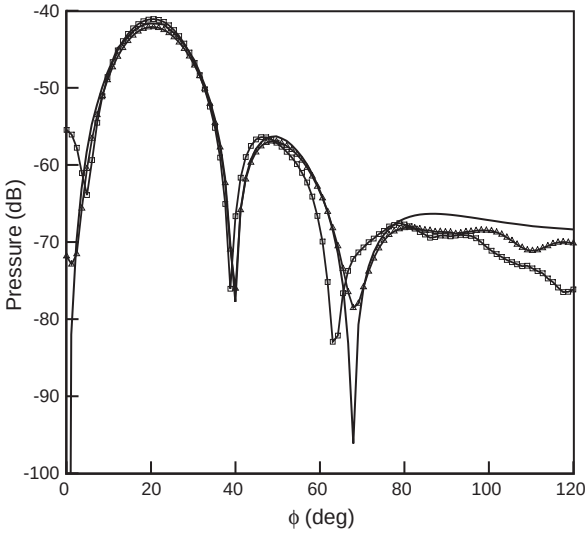

Fig. 12. Comparison of farfield directivity (10 PPW, $u_0 = 0$). Solid line: analytical solution; solid line with square: uniform grid; solid line with triangle: stretched grid.

with very low values which may relate to numerical truncating errors. It is clear that by using locally stretched grid with an average 10 PPW resolution the directivity prediction can be as good as that using 15 PPW on an uniform grid.

5. Concluding remarks

Certain issues in establishing a numerical method for duct acoustic radiation are addressed through a case study of planar wave radiation from a straight duct. The method is based on

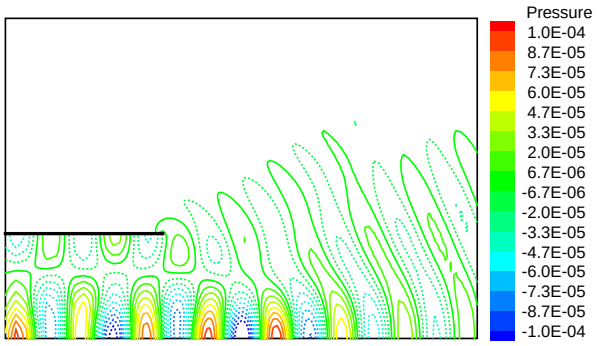

Fig. 13. Nearfield pressure using stretched grid (10 PPW, $u_0 = 0$).

solutions of linear Euler equations and the acoustic analogy. Comparisons of the farfield directivity with analytical solutions show good agreement. The main observations are:

1. Good performance of the buffer zone/admission zone is achieved. Strong damping and small wavefront angle are two main requirements for good performance. In practice, a buffer zone size of 20 cells (minimum 5 cells) may be sufficient for the duct propagation computation as wave reflections are determined by the cut-off ratio and the wavefront angle instead of PPW requirement.
2. The placement of the FW–H integration surface has only a marginal effect on the farfield directivity prediction.
3. The quality of the computation near the edge of the duct influences the farfield directivity prediction, especially in the angle prediction. Stretched grids increase local grid resolutions around the edge of the duct and give to the best predictions in both the farfield directivity and the sound pressure in the nearfield without mean flow. With a mean background flow, a stretched grid should be used with caution. For the unflanged duct case, a minimum 7 PPW can be used for the majority of the propagation area, but around the duct edge a high resolution of PPW > 15 should be adopted.

Acknowledgements

This work is performed under the EU project: TurboNoiseCFD, project number GRD1-1999-10509. The authors would like to thank J. Astley and B.J. Tester for helpful discussions during the study. Per Kruppa is the EU Technical Officer of the project.

References

[1] C.K.W. Tam, Computational aeroacoustics: issues and methods, *American Institute of Aeronautics and Astronautics Journal* 33 (1995) 1788–1796.
[2] Y. Özyörük, L. Long, Computation of sound radiating from engine inlet, *American Institute of Aeronautics and Astronautics Journal* 34 (5) (1996) 894–901.

[3] V.L. Wells, R.A. Renaut, Computing aerodynamically generated noise, *Annual Review of Fluid Mechanics* 29 (1997) 161–199.
[4] C.L. Rumsey, R.T. Biedron, F. Farassat, Ducted-fan engine acoustic predictions using a Navier–Stokes code, *Journal of Sound and Vibration* 213 (4) (1998) 643–664.
[5] W.Z. Shen, N. Sørensen, Aeroacoustic modelling of low-speed flows, *Theoretical and Computational Fluid Dynamics* 13 (4) (1999) 643–664.
[6] P.J. Morris, L.N. Long, A. Bangalore, Q. Wang, A parallel three-dimensional computational aeroacoustics method using nonlinear disturbance equations, *Journal of Computational Physics* 133 (1999) 271–289.
[7] V. Ahuja, Y. Özyörük, L. Long, Computational simulations of fore and aft radiation from ducted fans, AIAA Paper 2000-1943, 2000.
[8] S. Lidoine, H. Batard, S. Troyes, A. Delnevo, M. Roger, Acoustic radiation modelling of aeroengine intake comparison between analytical and numerical methods, AIAA Paper 2001-2140, 2001.
[9] G.F. Homicz, J.A. Lordi, A note on the radiative directivity patterns of duct acoustic modes, *Journal of Sound and Vibration* 41 (1975) 283–290.
[10] J.E. Ffowcs Williams, D.L. Hawkings, Sound generation by turbulence and surfaces in arbitrary motion, *Philosophical Transactions of The Royal Society, London* 246 (1969) 321–342.
[11] S.K. Richards, X. Zhang, X.X. Chen, P.A. Nelson, The evaluation of a buffer zone as an inflow/outflow boundary condition for computational aeroacoustic applications, *IMA Conference on Computational Aeroacoustics*, Greenwich, UK, April 2002.
[12] F. Farassat, G.P. Succi, The prediction of helicopter discrete frequency noise, *Vertica* 7 (1983) 309–320.
[13] R. Hixon, A new class of compact schemes, AIAA Paper 98-0367, 1998.
[14] F.Q. Hu, M.Y. Hussaini, J. Manthey, Low-dissipation and -dispersion Runge–Kutta schemes for computational acoustics, *Journal of Computational Physics* 124 (1996) 177–191.
[15] C.A. Kennedy, M.H. Carpenter, Comparison of several numerical methods for simulation of compressible shear layers, NASA Technical Paper 3484, 1997.